Contract No.:

This manuscript has been authored by Savannah River Nuclear Solutions (SRNS), LLC under Contract No. DE-AC09-08SR22470 with the U.S. Department of Energy (DOE) Office of Environmental Management (EM).

Controlled Release of Hydrogen Isotopes from Hydride-Magnetic Nanomaterials

Simona E. Hunyadi Murph,[*,†,§] *Kaitlin Coopersmith,*[†] *Henry Sessions,*[†] *Michael Brown*[†] *and George Larsen*[†]

†National Security Directorate, Savannah River National Laboratory, Aiken, SC USA

§Department of Physics and Astronomy, University of Georgia, Athens, GA USA

*Corresponding author, email address: Simona.Murph@srnl.doe.gov, phone: 803-646-6761

KEYWORDS: hydrogen absorption, hydride-magnetic nanomaterials, induced alternating magnetic field

ABSTRACT. In this work, hydrogen isotopes in the form of protium and deuterium were rapidly desorbed from magnetic-hydride iron oxide-palladium (Fe_2O_3-Pd) hybrid nanomaterials using an alternating magnetic field (AMF). Palladium, a hydride material with a well-known hydrogen isotope effect, was deposited on Fe_2O_3 magnetic nanoparticle support by solution chemistries and used as a hydrogen isotope storage component. The morphological, structural, optical, and magnetic studies reveal that the Fe_2O_3-Pd nanoparticles (NPs) are hybrid structures exhibiting both hydrogen isotope storage (Pd) and magnetic (Fe_2O_3) properties. The hydrogen isotope sorption/desorption behavior of metal hydride-magnetic nanomaterials was assessed by isothermal pressure-composition response curves (isotherms). The amount and rate of hydrogen isotope gas release was tuned by simply adjusting the strength of the magnetic field strength applied. Protium and deuterium displayed a similar loading capacity, namely H/M 0.55 and H/M=0.45, but different plateau pressures. Significant differences in the kinetics of release for protium and deuterium during magnetic heating were observed. A series of magnetically induced charge-discharge cycling experiments were conducted showing that this is a highly reproducible and robust process.

INTRODUCTION

As the world's energy demands continuously increase, the use of hydrogen and its isotopes as alternative sources of energy is attractive due to its renewability and sustainability. (1) For practical on-board applications, cheap and easy hydrogen storage and release must be realized. Hydrogen absorption and desorption using metal hydrides have been widely investigated for hydrogen storage, purification, and isotopic separation due to their high storage capacities and moderate desorption temperatures and pressures. (1-4) Additionally, the various hydrogen isotopes (tritium (T), deuterium (D) and protium (P)), have many applications in the medical field, nuclear energy, and defense missions. (5-7) Deuterium (D_2), one of the hydrogen's stable isotopes, is widely used in fission reactors, neutron scattering and as an isotope tracking marker in numerous chemical reactions. (8-10) Tritium, the only radioactive isotope of hydrogen, is a vital component of nuclear weapons, fusion reactors and self-illuminating light sources. (11) Tritium radioactively decays to helium-3, which is a highly sought constituent for detection of nuclear materials. The balance between deuterium and tritium is critical for fusion applications in the deuterium-tritium plasma system. (12) Isotopic mixtures of heavy water, D_2O, and tritiated water, T_2O, are also being processed yearly in thousands of tons for heavy water production for use as a moderator in nuclear reactors and tritium decontamination. (13) Isotopic separation is, however, not a trivial task as their physico-chemical properties are almost identical. Isotope separation have been demonstrated by several techniques including molecular sieving, (14) mass spectrometry, (15) laser ionization, (7, 16) cryogenic distillation processes, (17) thermal cycling absorption process (TCAP) (18) among others. Many of these approaches are inefficient, can be applied to only a limited number of isotopes, and require expensive technologies that are costly and maintenance intensive.

For practical applications, hydrogen absorption and desorption must be sufficiently fast, reversible, and energy efficient, without affecting material properties. A process that can produce

isotope effects, which leads to an isotope separation process, would be highly beneficial. Hydrogen absorption and desorption can often be slow in bulk hydride systems, due to the high enthalpy of formation and thermal effects. (19) To address some of these issues, alternate heating mechanisms for targeted heating to reduce temperature gradients and provide faster heat cycles should be explored. The metal-hydrogen interactions and ultimately their intrinsic kinetic behavior rely on the heat and mass transfer processes. Mass transport limitations in the bulk hydride systems can be overcome by using nanomaterials due to their unique chemical, physical, thermodynamic, and kinetic properties. (20) For example, nanoscale hydride materials display higher kinetics of gas uptake and release when compared with bulk materials and isotopic movement can be restricted and controlled at the nanoscale due to quantum size effects. (21, 22) Smaller scale materials also have increased surface areas and shorter diffusion distances for hydrogen movement and transfer, leading to increased diffusion-limited rates and faster hydrogen exchange rates. Quantum sieving for separation of hydrogen isotopes, either kinetic or chemical affinity quantum sieving, have been reported with 2D graphene sheets, boron-nitride membranes and metallic-organic framework materials. (8, 13, 23, 24) Moreover, protium and deuterium separation was demonstrated for nanoporous metal–organic frameworks MOF-74 by an advanced cryogenic thermal desorption spectroscopy (TDS) technique. (10) The interaction energies of the lighter hydrogen isotopes are weaker than the heavier isotopes because of the higher energies of the quantum states. (25, 26) Furthermore, the thermal de Broglie wavelength increases as the temperature and molecular mass are lowered. Ultimately, this speeds up the overall gas release process.

In this paper, we demonstrate that energy, in the form of an induced alternating magnetic field (AMF), is selectively coupled to hybrid magnetic-hydride Fe_2O_3-Pd nanomaterials for the selective and controlled release of hydrogen gas isotopes, namely protium and deuterium, while packed in

dry ice at -80 °C. The rate and amount of hydrogen isotope gas release can be manipulated by the selection of the magnetic field strength and the size of the coil. With a very small footprint, the proposed technology provides a safer method of precisely handling hydrogen isotopes stored in hydride materials.

RESULTS AND DISCUSSIONS:

Multifunctional nanomaterials:

A new class of multifunctional magnetic-hydride Fe_2O_3-Pd nanomaterials with hydrogen isotope gas storage capabilities were produced by solution chemistries. The reaction that decorates Fe_2O_3 nanoparticles (NPs) with palladium nanostructures is based on a classical metal ion reduction procedure reported by us earlier. (27-29) Fe_2O_3 nanospheres, with diameters of 70 ± 37 nm were used as "seeds" support for the palladium nanoparticle's growth. Scanning electron microscopy studies (**Figure 1 and SI - Figure S1**) show that the original spherical shape of the Fe_2O_3 materials remains intact after Pd nanoparticle's decoration. A fairly uniform decoration of the Fe_2O_3 "seeds" with quasi-spherical Pd particles with diameter of 27 ± 10 nm was achieved. Some cubic nanostructures with dimensions of 27 ±14 nm were also produced. The presence of cubic like particles, ≈10%, is not surprising as the preparation procedures involved the use of cetyltrimethylammonium bromide (CTAB), which is a known structure directing surfactant.(30, 31) The morphological, structural, optical, and magnetic studies performed on the resulting Fe_2O_3-Pd NPs reveal that they are hybrid structures exhibiting both hydrogen storage (Pd) and magnetic (Fe_2O_3) capabilities. Also, their magnetic properties remain intact after Pd decoration as shown in

Figure 2. When exposed to a magnetic field, the material is captured on the vessel's wall. Subsequent agitation leads to redispersion in the aqueous media.

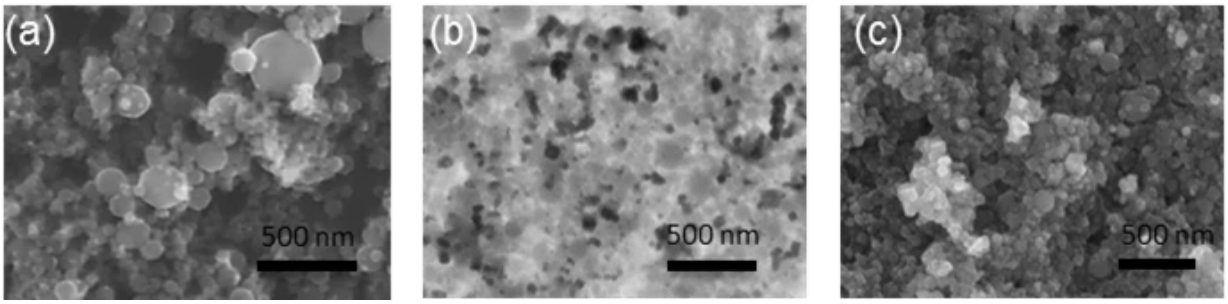

Figure 1. *SEM of* ***(a)*** *Fe_2O_3 and* ***(b)*** *Fe_2O_3-Pd nanostructures collected using backscattered electron imaging (Fe_2O_3 - grey; Pd - black);* ***(c)*** *Fe_2O_3-Pd nanostructures. Scale - 500nm.*

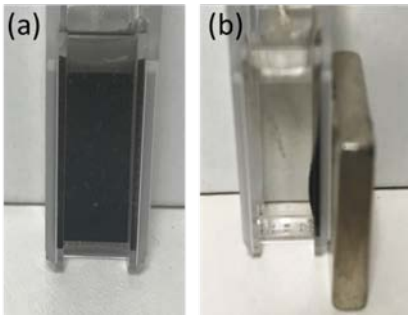

Figure 2. *Magnetic manipulation of the nanomaterial: (a) in solution and (b) under a magnet.*

To elucidate the compositional configuration of the hybrid Fe_2O_3-Pd NPs, X-ray energy dispersive microanalysis (EDS) was performed. EDS data (**Figure 3**) reveal that approximatively 27% Pd mol % was present on the Fe_2O_3 NPs support material. For a more quantitative analysis inductively coupled plasma mass spectrometry (ICP-MS) studies was performed confirming a percentage of 30% Pd mol % on Fe_2O_3 NPs. SEM studies (**Figure 1**) and EDS mapping (**Figure 3 b, c, d**) show that Fe_2O_3 decoration with Pd nanostructures did not occur on every individual Fe_2O_3 "seed" nanosphere. This is not surprising, as the original "seed" Fe_2O_3 NPs are magnetic

making them prone to aggregation before subsequent surface decoration. Previous X-ray diffraction reported by us reveals that the Fe_2O_3 spheres are in the maghemite phase (JCPDS 00-025-1402) with no preferred orientation. (29)

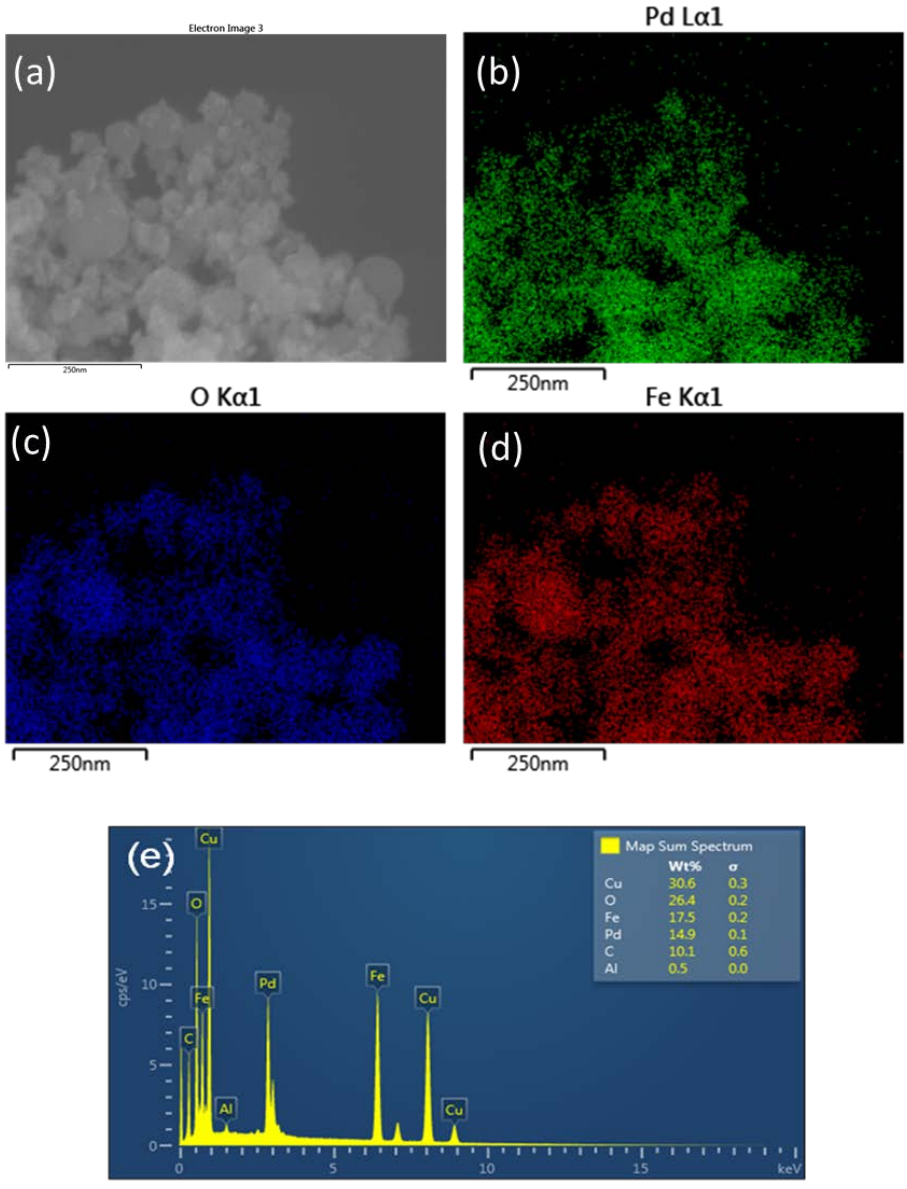

Figure 3. ***(a)*** *SEM image and* ***(b-d)*** *EDS mapping* ***(e)*** *EDS analysis for Fe_2O_3-Pd NPs.*

Zeta potential measurements were performed using phase analysis light-scattering to monitor the surface charge before and after the surface engineering experiments. The effective surface charge of the Fe_2O_3 NPs in DI water before decoration was negative with a value of – 11 mV. The negative surface charge is attributed to the electric potential formed at the solid support-liquid interface due to the presence of hydroxide ions adsorbed on the surface, specifically the deprotonated − Fe−OH species. Once immersed in the structure-directing surfactant CTAB, the Fe_2O_3 nanoparticles' surface charge significantly changes becoming highly positive, +19 mV. It is believed that an electrostatic interaction takes place between deprotonated $-O^-$ of the − Fe−OH species with the positive cetyltrimethylammonium headgroup. It is well documented in literature that the hydrophobic tails of CTAB interdigitate creating a "zipper" type bilayer on the nanoparticles surface. (27-32) This implies that the first cationic group is electrostatically binding at the nanoparticle's surface with the deprotonated $-O^-$ species, while the second cationic head group of the zipper-like structure of the CTAB is exposed to the environment, rendering it a positive surface charge. Once the Fe_2O_3 NPs surface is decorated with palladium nanostructures, additional changes arise. The surface charge of the Pd-Fe_2O_3 NPs decreased from +19 mV to +9 mV after Pd NPs decoration. These results suggest that CTAB is being partially removed from the surface during surface engineering process. Given that Pd decoration takes place at elevated temperatures, it is certainly possible that some CTAB is being destabilized and removed from the Fe_2O_3 surface leading to a less positive surface charge.

Performance Assessment of Magnetic Induced Heating Processes in Aqueous Systems

The nanoparticles' heating behavior under alternating magnetic fields (AMFs) were initially assessed in aqueous solutions. Specifically, to assess whether the NPs would heat in the presence of an alternating magnetic field, aqueous solutions of Fe_2O_3-Pd NPs were placed in the center of the coil of the magnetic induction system. The aqueous experiments were performed in the absence of hydrogen gases, e.g. protium or deuterium.

Theoretical simulations and mathematical calculations were conducted and revealed that the magnetic field strength at the center of the coil is about 1760 A/m. By using the Ansys Maxwell electromagnetic field simulation software, a magnetic flux density of 2.2 mT was determined as follows: (33)

$$B_{max} = \mu_0 nI \quad (1)$$

where μ_0 is the permeability of free space, n is the number of turns per unit length (N/l), and I is the current through the coil. (34)

The magnetic-induced heating responses for aqueous samples are found in **Figure 4**. Data shows a rapid temperature increase from t = 0 min until t = 15 min of the experiment with a heating rate of 4.1 °C/min for Fe_2O_3 and 3.6 °C/min for Fe_2O_3-Pd NPs. Once the temperature reaches around 45 °C, the temperature increase is less significant with a rate of 1.1°C/min for Fe_2O_3 and 2.0 °C/min for Fe_2O_3-Pd NPs. Subsequently, the temperature increases levels off at around 60 °C at t = 20 min. These solution-based experiments demonstrate that nanoparticles are heated via hysteresis and relaxation mechanisms instead of eddy currents, which is more typical of induction heating effects.

The specific loss power (SLP) or specific absorption rate (SAR) quantifies the amount of power transferred from the AMF into the environment through the excitation of the magnetic

nanoparticles. SLP is often calculated by taking the slope of the initially linear portion of the temperature versus time curve (**Figure 4**). However, this method does not take into account heat loss to the environment, nor the background heating of the temperature probe and the container. Thus, the SLP was also calculated by using the following exponential equation: (35)

$$T(t) = T_0 + \frac{SLP}{m_w c_w B}[1 - \exp[-Bt]] \quad (2)$$

where $T(t)$ is temperature at time t, T_0 is the initial temperature, SLP is specific loss power (in Watts), m_w is the mass of the water, c_w is the specific heat capacity of water. B is the rate of heat loss to the environment, and this parameter was determined by fitting the cooling curves after the AMF was turned off to the equation,

$$T(t) = A\mathrm{e}^{-Bt} \quad (3)$$

where A is the pre-exponential decay factor. Linear and exponential fitting curves were generated for the experimental data, and the obtained SLPs are listed in **Table 1**. SLPs of up to 1650 W g^{-1} have been measured for Fe_2O_3 NPs, which is comparable to values obtained for the Fe_2O_3 samples measured in this study. (36, 37) The temperature profile and SLPs are similar for both samples tested, with a less than 3-5% reduction in SLP when Fe_2O_3-Pd NPs was used. The small SLP reduction could be attributed to the material loss during sample preparation and purification. This demonstrate that the hybrid nanostructures retain their magnetic properties even after surface engineering. An IR camera was used to record the temperature profiles of the samples as depicted in SI (Figure S3).

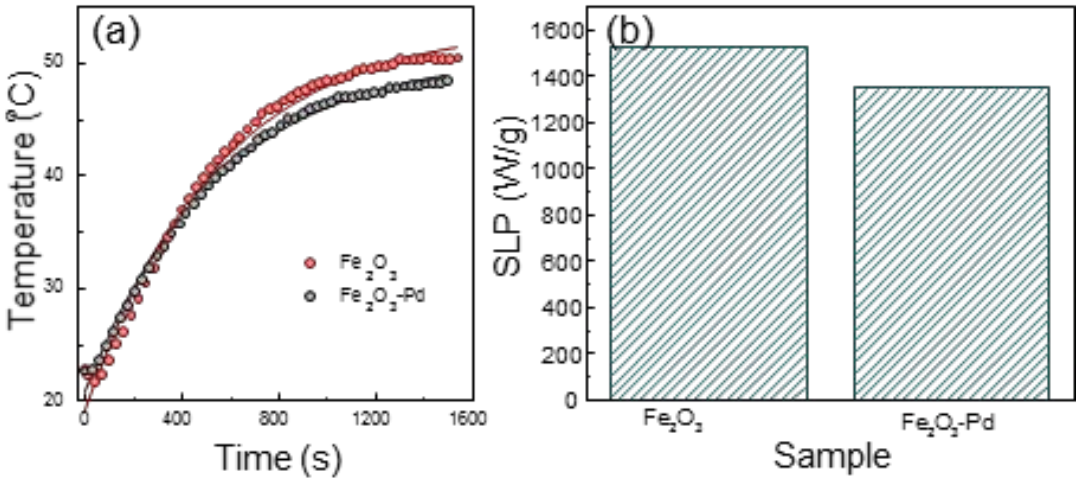

Figure 4. *AMF heating studies of Fe_2O_3 and Fe_2O_3-Pd NPs samples in aqueous solutions:* ***(a)*** *temperature profiles and* ***(b)*** *specific loss power (SLP).*

Table 1. SLP data for the Fe_2O_3 and Fe_2O_3-Pd nanoparticles obtained from exponential and linear fittings of the heating curve.

Nanoparticle Sample	**Exponential SLP (Watts/gram of Fe_2O_3)**	**Linear SLP (Watts/gram of Fe_2O_3)**
Fe_2O_3	1530 ± 50	1050 ± 20
Fe_2O_3-Pd	1350 ± 20	880 ± 10

Because the heating is homogeneous over the sample volume and there are no plasmonic effects, magnetic induction heating allows the use of the collective heating theory described by Keblinski et al. to evaluate the surface temperature rise at the Fe_2O_3 and Fe2O_3-Pd nanoparticles' surface. (38) According to the theory, there is no difference between the bulk temperature and the

nanoparticle surface temperature, except for the very short time period between when the alternating magnetic field is turned on and the time it takes for the temperature fields from the different nanoparticles to overlap, generally around a microsecond. The temperature rise on a nanoparticle's surface is given by

$$T(r,t) - T_\infty = \frac{dQ_{nano}/dt}{4\pi r\lambda}\left[\operatorname{erfc}\left(\frac{r-r_p}{2\sqrt{Dt}}\right) - \exp\left(\frac{r-r_p}{r_p} + \frac{Dt}{r_p^2}\right)\operatorname{erfc}\left(\frac{r-r_p}{2\sqrt{Dt}} + \frac{\sqrt{Dt}}{r_p}\right)\right] \qquad (4)$$

where r is distance from the particle center, T_∞ is the temperature far from the nanoparticle, dQ_{nano}/dt is the total power generated by a nanoparticle, λ is the thermal conductivity of the medium, D is the thermal diffusivity of the medium, r_p is the nanoparticle radius, and erfc denotes the complementary error function.

For nanoparticles dispersed in a solution, the bulk temperature rise of the system can be calculated by summing over all the individual nanoparticle contributions. To minimize computational effort, it is possible, as is done here, to consider a smaller inner region where Eq. 4 is explicitly evaluated for a smaller number of particles. Then, a homogenized result for a larger region can be added by numerical integration of Eq. 4. Furthermore, for our calculations, *dQnano/dt* was calculated per nanoparticle from the SLPs as determined in **Table 1**. **Figure 5a** shows the initial temperature rise (ΔT) on the surface of the nanoparticle. It is infinitesimal (note, the Log-Log scale), but happens very quickly. However, after less than a second, the temperature fields from the millions of nanoparticles begin to overlap, creating a large, homogenous bulk temperature rise. **Figure 5b** shows this collective heating effect and compares it to the experimental data. The model curve comes from integrating over the effects of millions of nanoparticles dispersed within a 2 cm diameter sphere within a volume of 8.4×10^{17} m^{-3}. These

results illustrate how the relatively small power input from an individual nanoparticle can produce large temperature changes in the bulk.

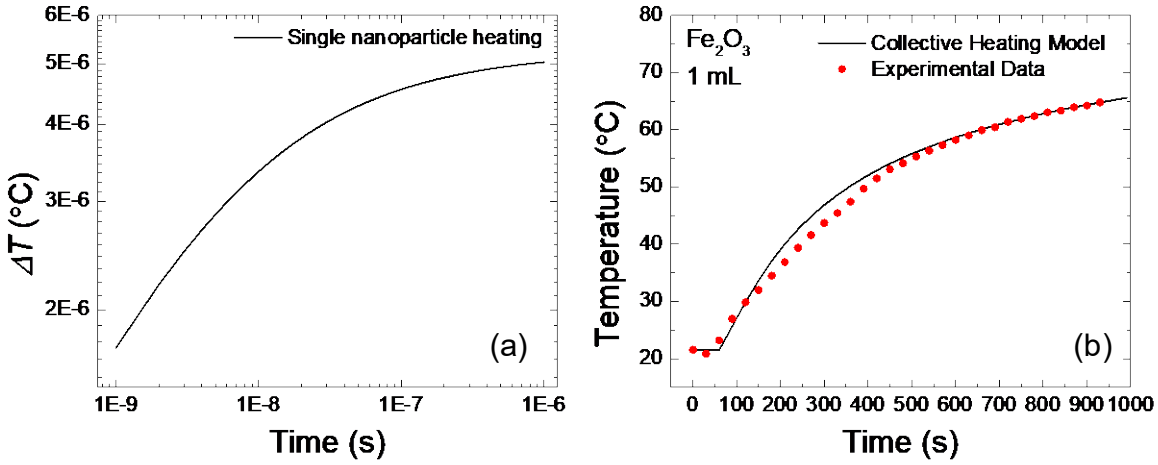

Figure 5. ***(a)*** *Calculated temperature rise on the surface of an individual Fe_2O_3 NP heated via AMF;* ***(b)*** *Comparison between experimental data and the calculated temperature rise within a Fe_2O_3 nanoparticle solution using the collective heating theory.*

Performance Assessment of Magnetic Induced Heating Processed in Gaseous Systems

Palladium has favorable properties that makes it highly sought for separation of hydrogen isotopes, separation of hydrogen from gas mixtures, and for hydrogen storage applications. (1, 4, 11) For example, palladium absorbs large volumetric quantities of hydrogen at room temperature and atmospheric pressure forming palladium hydride, PdH_x, exhibits rapid sorption kinetics, and can be easily activated. (39) Palladium also provides low temperature molecular hydrogen dissociation or decomposition, favorable thermodynamic properties, long-term cycling stability, and high reversibility at low temperature. (39) Hydrogen absorption by palladium and its alloys

have received considerable attention as these materials show large thermodynamic isotope effect on hydrogen absorption. (39-42) Hydrogen absorption/desorption by palladium is a reversible process. The absorption reaction is typically exothermic, and heat must be removed to sustain the process. On the other hand, the desorption reaction is endothermic, and heat must be provided to desorb the hydrogen from the hydride. As a result, a heating/cooling system is required for running an efficient process. The hydrogen storage capacity of a material, specifically the total hydrogen that can be absorbed by a material, is dependent on the hydrogen pressure and material's temperature. The higher the pressure and the lower the temperature, the higher its capacity. Subsequently, the heel of a system, namely the hydrogen left in a system after desorption, is dependent on pressure and temperature. A lower pressure but a higher temperature leads to a smaller heel. Therefore, the absorption pressure and temperature define the storage capacity, while the desorption pressure and temperature define the heel. The difference between the capacity and the heel is the operating or reversible capacity of the system. (18, 39, 40) Ultimately, the driving force responsible for the movement and subsequent release of the stored hydrogen gas in hydride materials relies on one's ability to precisely control the temperature gradients and pressure needed to perform the charging/discharging processes.

To evaluate the effects of AMF heating on hydrogen (protium or deuterium) gas absorption, aqueous solutions of nanomaterials Fe_2O_3-Pd and Fe_2O_3 NPs (**Figure 6a**) were loaded inside a glass capillary tube and subsequently dried. Upon drying at 80°C for 3-5 hours in air, the nanomaterials were deposited inside of the 0.16 cm diameter glass capillaries. **Figure 6b** shows photographs of the 10 cm long capillaries used in our studies. The Fe_2O_3 NPs loaded capillaries display an orange-brown color while the hydride-magnetic Fe_2O_3-Pd NPs had a dark brown-black

color. These colors of the dried samples in the capillaries were identical with the nanomaterial samples placed in aqueous solutions demonstrating that drying does not change their appearance.

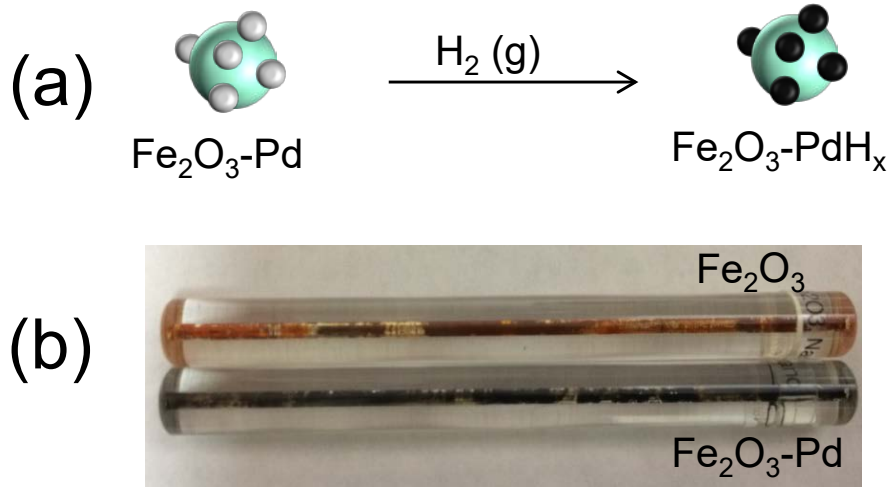

Figure 6. ***(a)*** *Schematic of hydrogen absorption;* ***(b)*** *Images of the Fe_2O_3 and Fe_2O_3-Pd NPs loaded capillaries.*

The materials in the freshly made capillaries were activated by exposing them to multiple hydrogen loading and unloading cycles to reduce available oxide groups in the iron oxide and palladium surfaces. Activation was deemed complete after the hydrogen absorption and desorption cycles and isotherms were reproducible and showed the expected hydrogen loading capacity. After hydrogen activation, the Fe_2O_3 capillaries turned from an orange color to black, indicating the reduction in the presence of hydrogen. The behavior of metal hydride/magnetic material is commonly assessed by isothermal pressure-composition response curves (isotherms) (**Figure 7**). A known amount of hydrogen gas, e.g. protium, deuterium, and/or tritium, is either introduced or withdrawn from the capillaries containing the hybrid magnetic-hydride nanomaterial at specific temperatures. When hydrogen gas is flown through capillaries containing Fe_2O_3-Pd, a metal hydride (PdHx) is created. The hydride material undergoes a phase transition (α→β or vice versa)

as hydrogen is either interstitially incorporated or removed from the Pd lattice (**Figure 7**). (43) Successive hydrogen additions produce an absorption isotherm, whereas a series of removals produces a desorption isotherm. Once a solid-gas equilibrium is achieved, the pressure is measured. The difference in headspace pressure in the sample before and after exposure to hydrogen is used to calculate the amount of gas absorbed or desorbed from the hydride. Due to hysteresis, the absorption plateau is at a slightly higher pressure than the desorption plateau. The length and slope of the transition plateau region is indicative of the capacity and homogeneity of the hydride, respectively. The solid phase composition is normally presented as the ratio of hydrogen atoms to metal atoms.

To determine the loading capacity of the Fe_2O_3-Pd NPs, isotherms were collected for H_2 in the form of protium. As shown in **Figure 7**, the plateau pressure at room temperature for the multifunctional Fe_2O_3-Pd NPs was ≈10 Torr, with a calculated capacity of 0.55 H/M for protium. This is comparable to literature values for palladium nanoparticles of around 0.50 H/Pd. (44, 45) The kinetics of hydrogen absorption is dependent on nanoparticle's size, shape and composition. (44, 46)

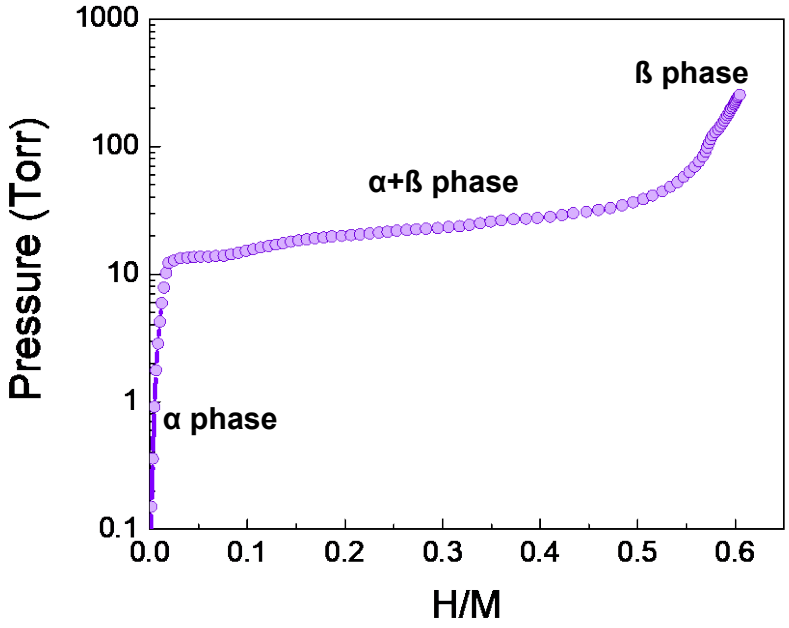

Figure 7. *Pressure-composition absorption isotherm for Fe_2O_3-Pd NPs for protium at room temperature.*

Once the NPs are placed under H_2 atmosphere, in this case protium, the absorption/desorption was monitored using pressure transducers attached to the capillaries. The capillaries were initially cooled by using dry ice in order to increase the amount of protium stored in the Pd NPs. While still under dry ice storage, the capillaries were heated by an AMF (3.7 mT, power = 80%), and the subsequent change in pressure was measured over time. The results for the Fe_2O_3 NP and Fe_2O_3-Pd NP capillaries are shown in **Figure 8a**. As expected, an increase in pressure for the Fe_2O_3 NPs was observed, and this is due to the change in headspace pressure with increasing temperature ($P = nRT/V$) as a result of the AMF heating of the NPs. A larger (**Figure 8b**) and faster pressure increase (**Figure 8c**) was measured for the Fe_2O_3-Pd NPs of the same concentration, even though a slightly lower SLP was obtained for the hybrid NPs. The larger pressure swings for the Fe_2O_3-Pd NPs are due to a combination of both the increase in headspace pressure from AMF heating

and due to the protium release from the solid phase into the gaseous phase. Notably, the pressure also increased as soon as the AMF was turned on, indicating that the gas release and/or the local NP temperature response to the AMF is immediate, which is much faster than would occur with traditional heating methods (i.e. electrical heating). In **Figure 8a**, it is also worth noting that the baseline pressure for the Fe_2O_3-Pd capillary slightly increased over time, while the baseline pressure in Fe_2O_3 NPs remained relatively constant. This is because the capillary tubes cool faster and the protium can be re-adsorbed back into the Pd lattice. A direct comparison with palladium nanostructures was not possible due to lack of ferromagnetic properties. As a result, heating under an alternating magnetic field was not possible. However, protium isotherm data for Pd nanoparticles with dimensions < 25nm in diameter under obtained conventional heating method are available in the SI (Figure S2).

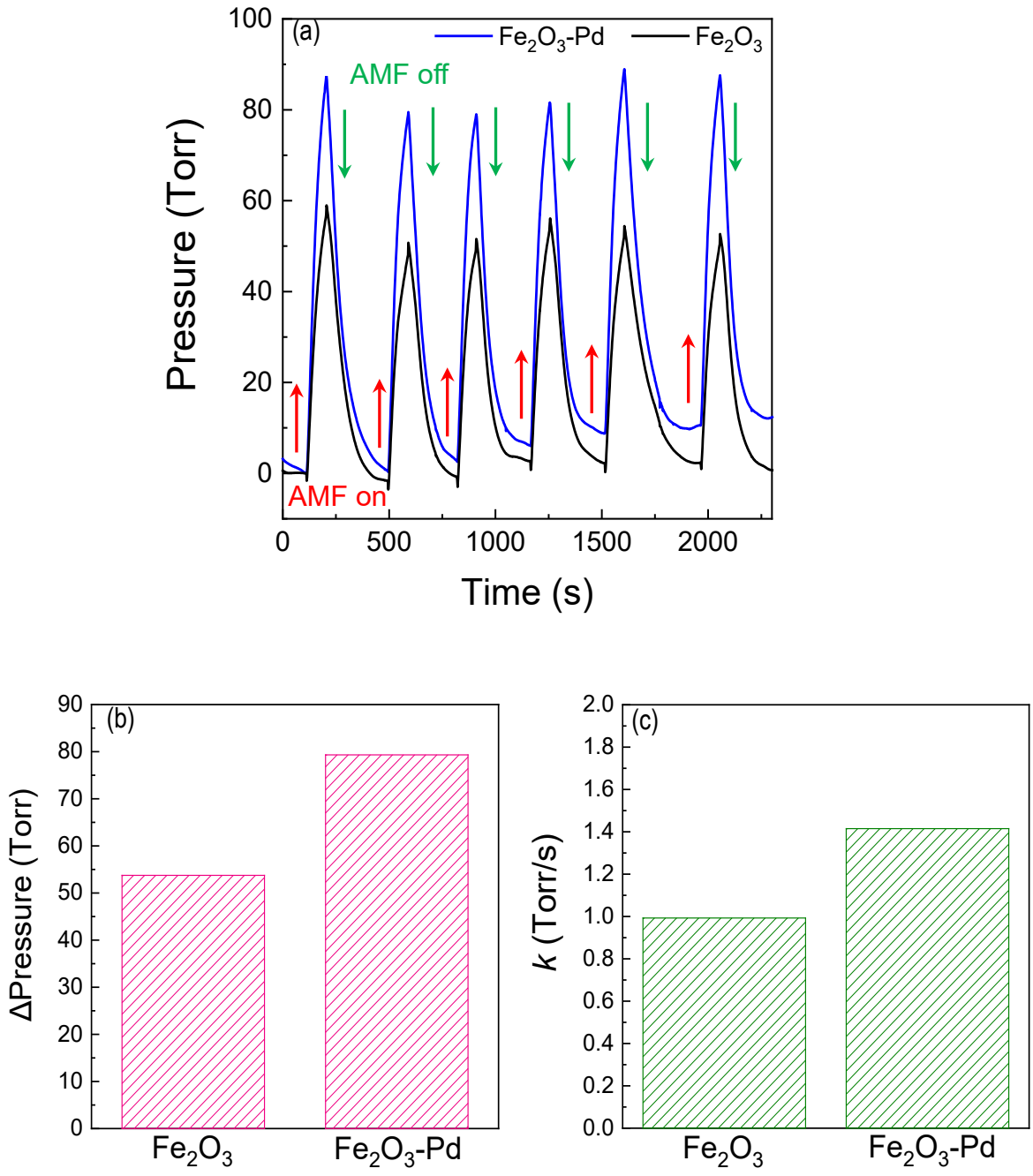

Figure 8. ***(a)*** *Change in pressure for magnetic heating cycles for Fe_2O_3 and Fe_2O_3-Pd NPs capillaries loaded with H_2 to P_i=930 Torr:* ***(b)*** *Change in pressure and* ***(c)*** *Rate of pressure change for the Fe_2O_3 and Fe_2O_3-Pd NPs capillaries. (Data is offset to zero).*

To confirm that the increased pressure swings for Fe_2O_3-Pd NPs is due to gas release, a series of control experiments were performed with He gas to measure the pressure differences when neither nanomaterial absorbs the carrier gas. As shown in **Figure 9**, the change in pressure between the two capillaries was very small ($\Delta P = 2$ Torr), whereas with the protium gas the change in pressure between the two capillaries was significantly larger ($\Delta P = 25$ Torr), which corresponds to a release of 0.3 μmol P_2 using ΔP. These data confirm that the larger difference in pressure between the two capillaries in a protium atmosphere is due to the absorption and desorption of protium in the AMF. The slight difference between the two capillaries is due to the greater SLP for the Fe_2O_3 particles, as seen in **Table 1** and **Figure 4**.

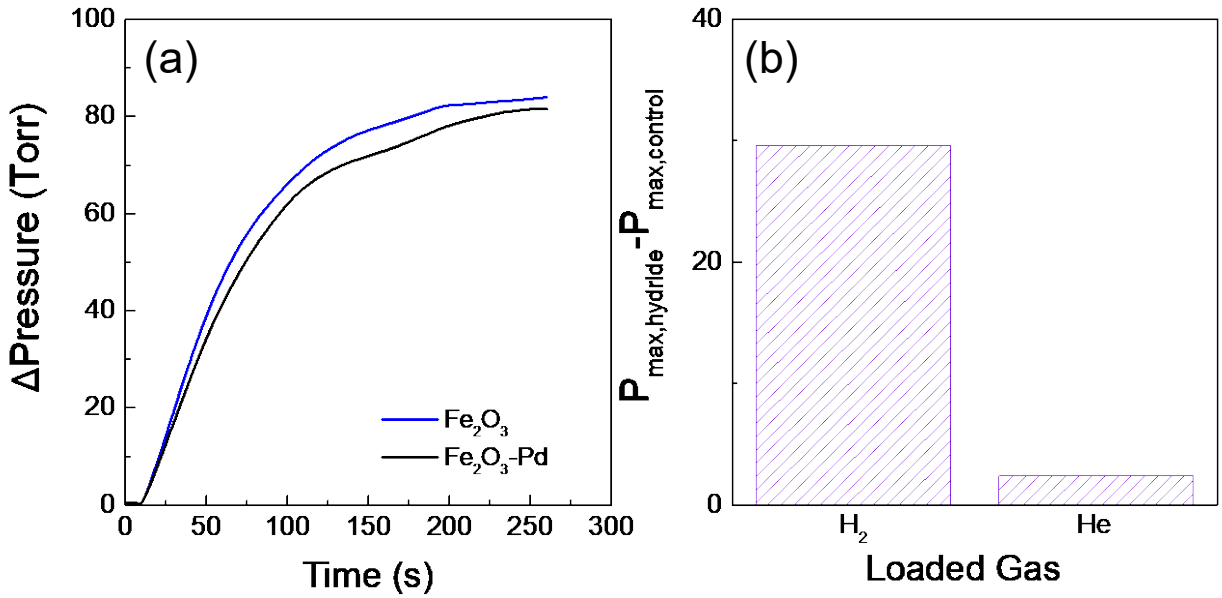

Figure 9. ***(a)*** *He loaded capillaries****; (b)*** *Difference between the Fe_2O_3 and Fe_2O_3-Pd capillaries for He and H_2 (in the form of protium) loading.*

A change in pressure occurred even after the capillaries were evacuated prior to AMF exposure (**Figure 10**). In **Figure 10**, the pressure of the Fe_2O_3-Pd capillary increased 75 Torr in response to the AMF, whereas the pressure for the Fe_2O_3 control showed a very small increase of only 1 Torr. Since this sample was evacuated, the presence of protium in the overhead gas is minimal, leading to a pressure increase due to protium desorption rather than a pressure response with minimal change in overhead pressure due to temperature. This change in pressure corresponds to a release of 0.9 μmol protium for the Fe_2O_3-Pd sample. The small pressure increase of Fe_2O_3 may be due to the release of surface water and residual gases during heating.

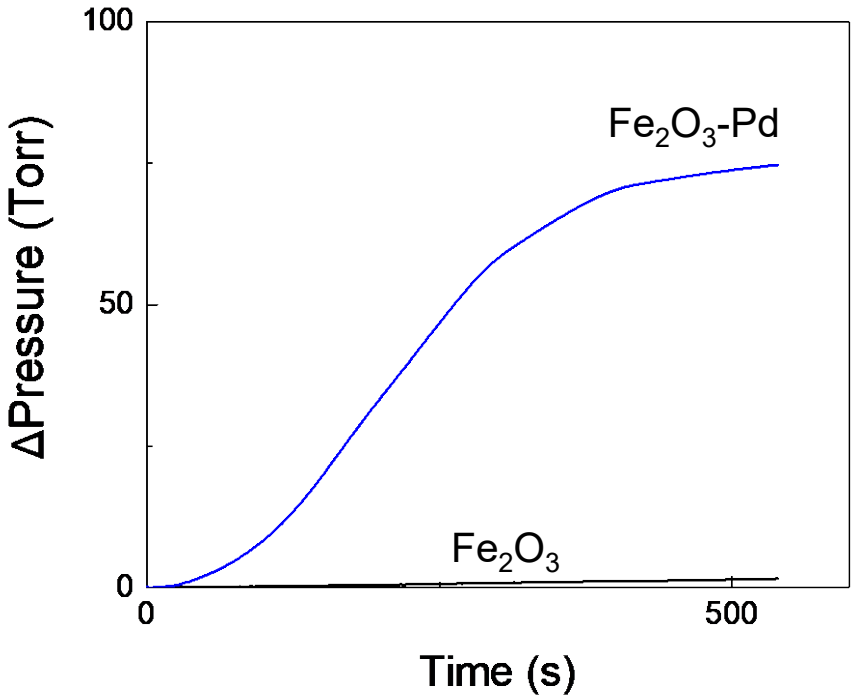

Figure 10: *Protium cycling with capillaries while under vacuum (P_i=1 Torr). Data is offset to zero.*

The hydrogen desorption performance of $LaNi_5$ hydride materials under an electromagnetic induction field has been reported by Belkhiria et al. (47) The authors' show that, the reaction times, thermal equilibrium and the dissipated energy are considerably reduced when an electromagnetic

induction heating system is used in comparison to a traditional fluid heating method. Our studies here indicate that a hydride material can be combined with a magnetic material to create a multifunctional structure with similar benefits, but with the additional advantages of being able to separately optimize the performance of the individual components (e.g., SLP, plateau pressure, etc.).

Controlled release of protium gas

The effect of magnetic strength on protium release kinetics from the Fe_2O_3-Pd NPs was measured (**Figure 11**) by controlling the magnetic field strength, namely AMF power, and monitoring the pressure in the capillary. The pressure increase trend is similar in all cases and is highly dependent on the applied AMF power. As the AMF power increased from $0.4x10^{-3}$ to $2.73x10^{-3}$ T, the pressure increased from 460 Torr to 750 Torr. The pressure profile rose incrementally from 9.8 Torr/sec to 109.1 Torr/sec, indicating that, as the magnetic field strength increased, more protium gas was being released (**Figure 11b**), from 3.4 μmoles to 5.3 μmoles. The increasing slope with increasing magnetic field strengths also indicates faster kinetics of protium release with increasing AMF power. During the experiments, the temperature on the outside of the capillary reached as high as 112 °C, which was measured using an infrared camera placed 10 cm from the vessel (**Figure 11a inset**); however, the temperature within capillary in proximity of the NPs is higher. These results are highly encouraging as one could easily control any fluids sorbed on magnetic or magnetic-hybrid nanomaterials of interest by the simple use of an alternating magnetic field.

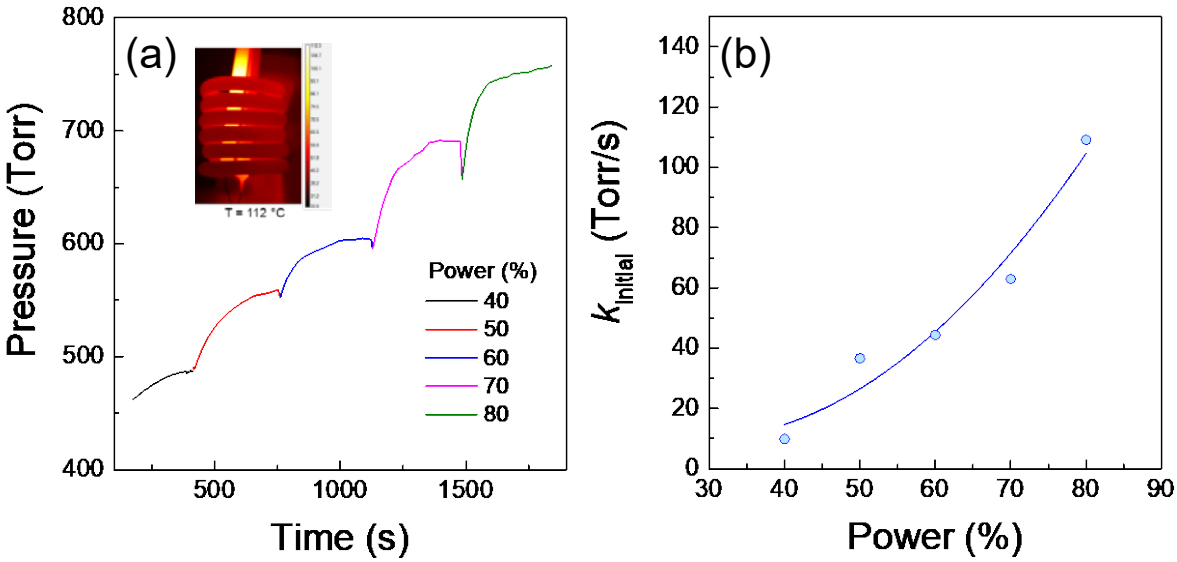

Figure 11. ***(a)*** *Change in pressure with increasing current; (inset) infrared thermal image of the capillaries during magnetic heating;* ***(b)*** *Change in pressure as a function of magnetic field strength.*

Isotopic effects under an alternating magnetic field

After protium isotherms were collected, a series of deuterium isotherms were performed to determine the existence of any isotopic effect, between those species. **Figure 12** shows a comparative example of protium and deuterium pressure-composition isotherm for Fe2O3-Pd NPs after activation of nanoparticles. Each isotherm shows the typical α, β, and α+β phases. Distinct plateau pressure where observed between protium and deuterium. Compared to the protium isotherm, the deuterium isotherm showed a slightly lower capacity (H/M=0.45) and a higher plateau pressure. This is not surprising since the equilibrium pressure of each isotope is based on the thermodynamics between Pd and isotope of interest. (42) For example, a recent study reported activation energy values of 18.63 kJ mol^{-1} for protium and 15.79 kJ mol^{-1} for deuterium suggesting that the internal diffusion of each isotope contributes to isotopic effects. (48) Another study

showed that the activation energy of desorption for deuterium was smaller than that for protium on palladium. (40) This was attributed to the difference in the enthalpy between protium and deuterium absorption into metal. Parida's group also reported a hydrogen isotope effect between deuterium and protium on palladium-based alloys. Specifically, the deuterium equilibrium plateau pressures were higher than the corresponding protium equilibrium pressure at all temperatures investigated. (41)

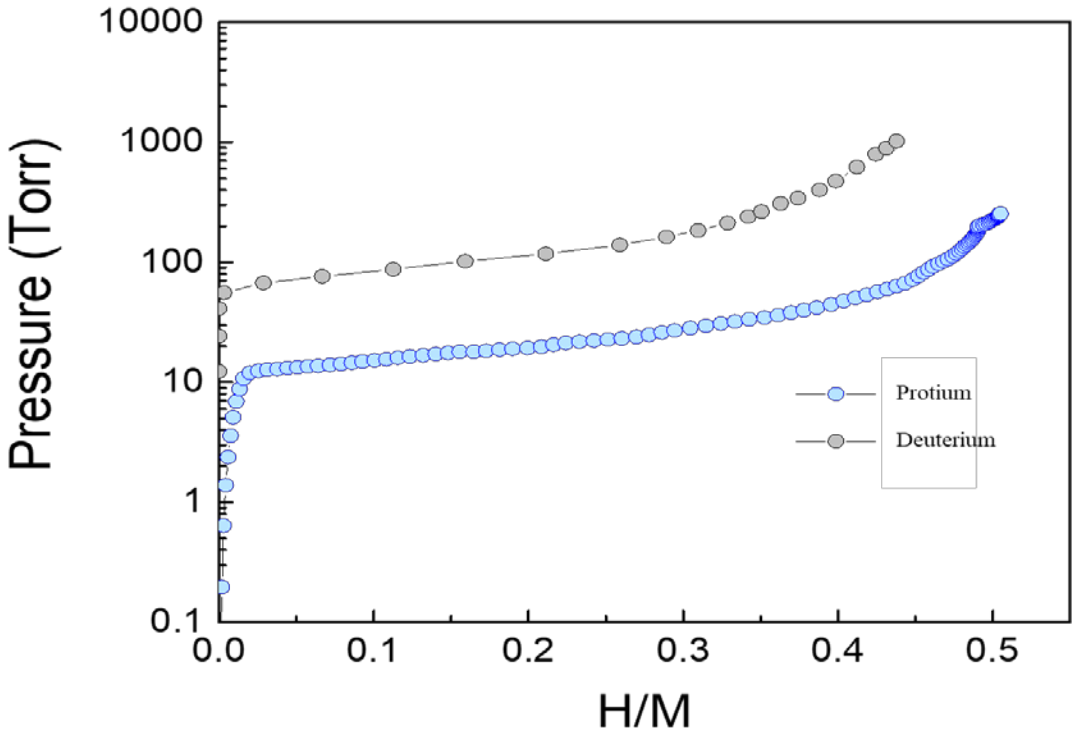

Figure 12. *Protium (blue) and deuterium (gray) pressure-composition absorption isotherms for Fe_2O_3-Pd NPs at room temperature.*

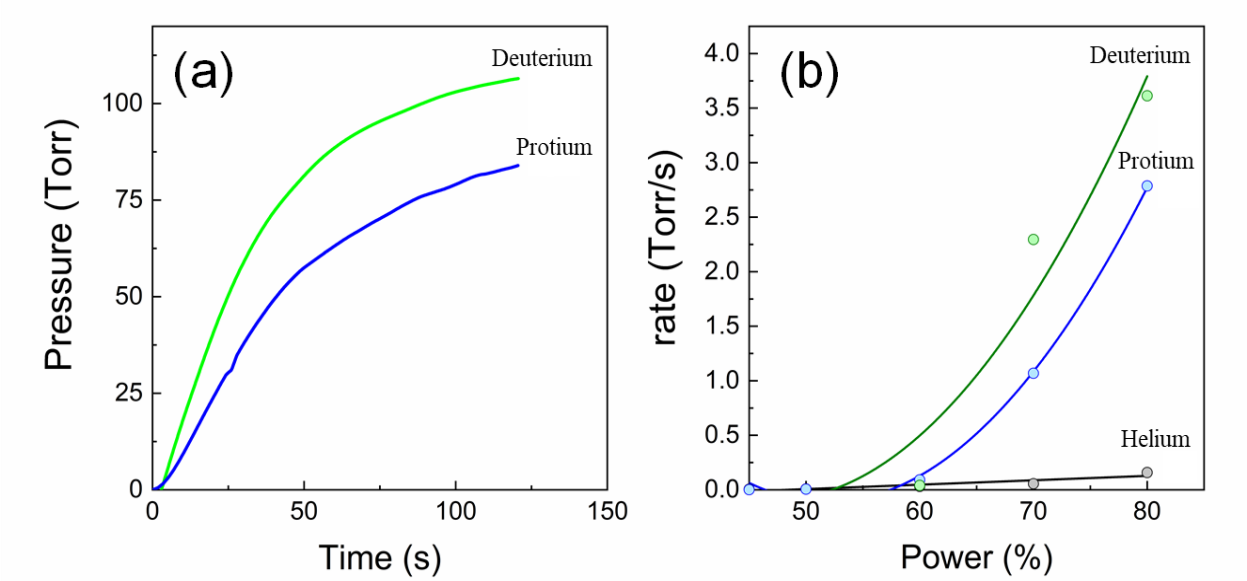

Figure 13. ***(a)*** *Heating cycles for deuterium and protium at 70% magnetic power;* ***(b)*** *Kinetic effects on the magnetic desorption of protium, deuterium, and helium.*

The isotopic effect on the pressure curves was measured (**Figure 13a**), showing a higher increase in pressure for the deuterium loaded capillary. Correspondingly, the rate of release (**Figure 13b**) also shows a faster release for deuterium compared to protium, which is expected based on the kinetic isotope effect. (40-42, 44) It is important to note that the relative rate (Torr/s) for deuterium desorption versus protium desorption deviates from an ideal value of 1.4, which one would expect based on the square root of the relative masses. (40) These deviations can be attributed to gas heating in the headspace for different over-pressures. Compared to traditional methods of hydrogen separation, employing magnetic heating is more efficient since magnetic heating is more targeted, and therefore faster than electric heating.

CONCLUSIONS

A new class of multifunctional magnetic-hydride Fe_2O_3-Pd nanomaterials with hydrogen storage capabilities and isotope effects were produced by solution chemistries. The morphological, structural, optical, and magnetic studies reveal that the Fe_2O_3-Pd nanoparticles (NPs) are hybrid structures exhibiting both hydrogen storage (Pd) and magnetic (Fe_2O_3) properties. Exponential and linear specific loss power (SLP) data was generated on Fe_2O_3 and Fe_2O_3-Pd nanoparticles from the collective heating theory. The temperature profile and SLPs are similar for both samples tested, namely 1530 ± 50 W g^{-1} and 1350 ± 20 for Fe_2O_3 and Fe_2O_3-Pd NPs, respectively. The small reduction of less than SLP 3-5% determined for Fe_2O_3-Pd NPs was attributed to material loss due to purification and transfer. The collective heating theory of Keblinski was used to calculate the temperature increases that arise from the small power input from an individual nanoparticle. The model curve shows that, within seconds, the temperature fields from the millions of nanoparticles begin to overlap, creating a large, homogenous bulk temperature rise. The collective heating theory was confirmed by the experimental data. To determine the loading capacity of the Fe_2O_3-Pd NPs, isotherms were collected for hydrogen isotopes, namely protium and deuterium. The data show that the plateau pressure at room temperature for the multifunctional Fe_2O_3-Pd NPs was ≈10 Torr, with a calculated capacity of 0.55 H/M for protium which agrees with previous studies. Compared to the protium isotherm, the deuterium isotherm shows a slightly lower capacity (H/M=0.45) and a higher plateau pressure. Significant differences in the kinetics of release for H_2 and D_2 during magnetic heating were observed. This demonstrates that the known isotopic effect in Pd is preserved in multifunctional magnetic-hydride Fe_2O_3-Pd nanomaterials during interaction with an AMF. A series of magnetically induced charge-discharge cycling experiments were conducted showing that this is a highly reproducible and robust process.

Materials and Instrumentation

Materials: Sodium tetrachloroplatinate (Na_2PdCl_4), hexadecyltrimethylammonium bromide (CTAB), trisodium citrate, ascorbic acid (AA), Pd nanoparticles and Fe_2O_3 nanospheres were purchased from Sigma-Aldrich and used as received. All aqueous solutions were prepared in deionized water.

Instrumentation: The Brookhaven Instruments DLS NanoBrook Omni (110-240 V) was used to confirm NPs hydrodynamic radius and surface charge (Zeta potential). A Hitachi SU8200 Scanning Electron Microscope (SEM) coupled with EDS capability was used to determine NPs morphologies and semi-quantitative compositions. An in-house fabricated, manual Sieverts apparatus was designed and built to measure the gas absorption-desorption behavior of small quantities of hydride material at low pressures (~0 to 1200 Torr). The apparatus only allowed for manual operation of the valves to deliver a known quantity of gas to the hydride material but was later upgraded to an automated system. Volume calibrations of the Sieverts apparatus were performed using helium (He) in a calibrated volume (26 cc). The apparatus can process two samples concurrently for determination of equilibrium temperatures, pressures, and thermodynamics. 10 cm long capillary sample tubes were connected to the Sieverts apparatus using 0.05 mm capillary tubes connected to the automated valve on the apparatus. Paroscientific pressure transducers were connected to the inlet side of the capillaries. The sample tubes were also equipped with NovaSensor PTs to measure the gas on the outlet of the capillary. The NovaSensor PTs were connected to an in-house fabricated circuit board to amplify the signal from the transducers for data acquisition. This apparatus is capable of collecting multiple absorption-desorption experiments at various temperatures to study long-term cycling effects on capacity and kinetics. The temperature of the induction heating system was monitored using a FLIR SC645

model infrared (IR) camera (temperature measurement range: -20°C to 2000°C, accuracy ± 2%; 24.6 mm focal length; 0.69 mrad spatial resolution) mounted to the side of the induction vessel to record the temperature during heating.

Experimental Section

(a) Fe_2O_3-Pd NPs preparation: Pd nanoparticles were produced by reduction approaches as previously reported by us while using Fe_2O_3 NPs as seed supports Briefly, 0.125 mmoles Fe_2O_3, 0.08 mmol CTAB, 0.12 mmoles Na_2PdCl_4 in 20 mL DI H_2O was heated to 80 °C before 0.14 mmoles L-ascorbic acid was added. Solution turned black immediately. The solution was heated at 80 °C for 30 minutes before being cooled and magnetically purified three times. The final Fe_2O_3-Pd materials were suspended in water.

(c) Fe_2O_3 and Fe_2O_3-Pd NPs Capillary Loading: Aqueous solutions containing 17 mg of Fe_2O_3 or Fe_2O_3-Pd NPs were injected into capillary tubes. The cleaned NPs were loaded into capillaries in water and dried in an oven at 80 °C. The dried capillaries containing NPs of interest were subsequently sealed to a circuit with a pressure transducer using epoxy. Hydrogen, either protium or deuterium, activation was carried out by loading the capillaries with hydrogen to 1500-2000 Torr and exposed to multiple heating and cooling cycles until hydrogen absorption occurred. The capillaries were cooled using dry ice then warmed up to room temperature and heated with the alternating magnetic induction heater and then evacuated. For the gas desorption studies, the capillaries were loaded with hydrogen gas and then cooled using dry ice. While on dry ice, the capillaries were heated with the alternating magnetic induction heater.

(d) Alternating magnetic field device: A magnetic hyperthermia system with a 6-turn coil (17.5 mm radius and 47.5 mm height) was purchased from MSI Automation, Inc. Alternating magnetic fields at 425 kHz were generated by controlling the power to the coil. Magnetically induced heating experiments were conducted on aqueous solutions of Fe_2O_3 and Fe_2O_3-Pd MNPs. A Neoptix fiber optic temperature probe was used to monitor the temperature gradients in the solution. The MNPs were then placed inside the center of the coil of the magnetic hyperthermia system (Power = 80%). The magnetic induction experiments were performed in an oscillating magnetic field at different magnetic field strengths, which were controlled by changing the percent of full-scale power, which influenced the amount of current supplied to the coil. The relationship between magnetic field strength and current is shown in equation 1:

$$B = \mu nI \qquad \text{(Equation 1)}$$

Where B is magnetic field strength, μ is magnetic permeability (1.26×10^{-6} H/m for Cu coil), n = turns/meter (6 turns in 4.5 cm; n = 133 turns/m), and I is current (Amps). Table 2 shows the magnetic field strength of the magnetic induction system at the various tested power levels.

Table 2. Magnetic strength calculated from the power settings and current for the induction heater

Power Setting (%)	**Current (Amps)**	**B (Tesla)**	**B (Gaussian)**
40	2.4	4.02×10^{-4}	4.0
50	6.4	1.07×10^{-3}	10.7
60	9.9	1.66×10^{-3}	16.6
70	13.3	2.23×10^{-3}	22.3
80	16.3	2.73×10^{-3}	27.3

(e) Magnetic induction studies in water: To assess whether that the nanomaterials would heat in the presence of a magnetic field, aqueous solutions of Fe_2O_3 or Pd- Fe_2O_3 materials were placed in the center of the coil of the magnetic induction system at room temperature. The magnetic heating was measured at 60%, 70% and 80% power. The temperature was measured using a Neoptix temperature probe.

(f) Isotherm collection: Isotherms were collected at room temperature (294 K). The pressure increase of the capillaries were monitored as known aliquots (9-600 µL) of P_2, D_2 and He gases were added using a in house built sievert system. He calibrations were carried out to determine the volume of the valves and the capillary. At a given temperature, a known amount of gas was either introduced or withdrawn from the system containing the hybrid magnetic-hydride nanomaterial and the pressure was measured after a new solid-gas equilibrium is achieved. The difference in pressures before and after exposure of hydrogen to the sample allows one to calculate the amount of gas absorbed or desorbed from the hydride. Prior to magnetically induced heating experiments, the samples are loaded with hydrogen, either protium or deuterium, at room temperature, then placed in a dewar with dry ice (at -78 °C). This allows the hydrogen gas present in the headspace to be absorbed by the hydride material. Once the capillaries are loaded, they are kept under hydrogen pressure. The pressure gradients are monitored using pressure transducers. The absorption/desorption experiments are conducted remotely and induced through an alternating external magnetic field, which heats the hydride nanomaterials. The pressures in the capillaries were well below 7600 Torr, where the ideal gas law for H_2 is still valid; therefore, the concentration of the gas inside of the capillary at room temperature was calculated using the ideal gas law. Using the pressure and the volume of the capillary, the concentration of P_2 gas in the overhead pressure inside of the capillaries before magnetic heating was calculated to be 9.6 µmol (V_{cap}=130 µL; P=

894 Torr) for these experiments in dry ice. For the D_2 experiments, the concentration of D_2 in the overhead pressure prior to magnetic heating was 8.2 μmol (V_{cap}=130 μL; P= 757 Torr).

(e) Magnetic gas release: The capillaries were loaded to the plateau pressure (~10-100 Torr) with H_2, D_2 and H_2/He gas mixtures and incubated until the pressure stabilized. The capillaries were then cooled on dry ice and heated with the alternating magnetic induced heater with varying currents (4-17 amps).

Author Contributions

The manuscript was written through contributions of all authors. All authors have given approval to the final version of the manuscript.

Funding Sources

This work was supported by the Laboratory Directed Research and Development (LDRD) program within the Savannah River National Laboratory (SRNL). This document was prepared in conjunction with work accomplished under Contract No. DE-AC09-08SR22470 with the U.S. Department of Energy (DOE) Office of Environmental Management (EM).

ACKNOWLEDGMENT

We appreciate Mr. Charles Shick's support by providing the ICP-MS data on our samples.

Supporting Information

The supporting information contains additional SEM images of Fe_2O_3-Pd nanostructures, SEM images collected using backscattered electron imaging of Fe_2O_3-Pd nanostructures, protium isotherm on palladium nanoparticles, photographs and IR heating rate and thermal energy balance profiles of aqueous solutions of Fe2O3 NPs and calculation of hydrogen concentration.

REFERENCES

1. Rusman, N. A. A., Dahari, M. A Review on the Current Progress of Metal Hydrides Material for Solid-State Hydrogen Storage Applications *Int. J. Hydrog. Energy,* **2016**, *41*, 12108-12126.
2. Wang, L., Rawal, A., Aguey-Zinsou, K. Hydrogen Storage Properties of Nanoconfined Aluminum Hydride (AlH_3) *Chem. Eng. Sci.,* **2019**, *194*, 64-70.
3. Mazur, T.R., Klappauf, B., Raizen, M.G. Demonstration of Magnetically Activated and Guided Isotope Separation *Nature Physics,* **2014**, *10*, 601- 605.
4. Jin, Y., Wang, L., Hara, M. Watanabe, K. Kinetics of Hydrogen Isotope Absorption for Well-Annealed Palladium-Platinum Alloys *Materials Transactions,* **2007**, *48*, 560 -565.
5. Sanderson, K. Big Interest in Heavy Drugs *Nature*, **2009,** 458, 269-270.
6. Smith, R., Whittaker, D. A. J., Butler, B., Hollingsworth, A., Lawless, R.E., Lefebvre, X., Medley, S.A., Parracho, A.I., Wakeling, B., Hydrogen Isotope Separation for Fusion Power Applications *J. Alloys Compd.,* **2015**, *645,* 51-55.
7. Jerkins, M., Chavez, I., Even, U., Raizen, M.G., Efficient Isotope Separation by Single-Photon Atomic Sorting *Phys. Rev. A,* **2010**, *82,* 033414.
8. Niimura, S., Fujimori, T., Minami, D., Hattori, Y., Abrams, L., Corbin, D., Hata, K., Kaneko, K., Dynamic Quantum Molecular Sieving Separation of D2 from H2–D2 Mixture with Nanoporous Materials *J. Am. Chem. Soc.,* **2012**, *134*, 18483 -18486.
9. Cai, J., Xing, Y., Zhao, X., Quantum Sieving: Feasibility and Challenges for the Separation of Hydrogen Isotopes in Nanoporous Materials *RSC Adv.,* **2012**, *2*, 8579 - 8586.

10. Oh, H., Savchenko, I., Mavrandonakis, A., Heine, T., Hirscher, M Highly Effective Hydrogen Isotope Separation in Nanoporous Metal Organic Frameworks with Open Metal Sites: Direct Measurement and Theoretical Analysis *ACS Nano,* **2014**, *8,* 761-770.

11. Tosti, S., Ghirelli, N. Tritium in Fusion: Production, Uses and Environmental Impact Nova Science Pub Inc; UK ed. Edition, May 1, **2013**, ISBN-13: 978-1624172700.

12. Dolan, M.D., Lamb, K.E., Evtimova, J.B., Viano, D.M. Deuterium Enrichment using Vanadium Membranes *Intern. J. Hydrogen Energy,* **2017**, *42*, 24183-24188.

13. Lozada-Hidalgo, M., Zhang, S., Hu, S., Esfandiar, A, Grigorieva, I.V., Geim, A.K. Scalable and Efficient Separation of Hydrogen Isotopes using Graphene-based Electrochemical Pumping *Nature Communications,* **2017***, 8*, 15215.

14. Kim, J.K., Oh, H., Moon, H.R. Hydrogen Isotope Separation in Confined Nanospaces: Carbons, Zeolites, Metal–Organic Frameworks, and Covalent Organic Frameworks *Adv. Mater.* **2019**, *31*, 1805293.

15. Liezers, M., Dion, M.P., Eiden, G.C., Thomas, M.L.P. Quantifying Low-Energy ICP-MS Isotope Deposition *J. Anal. At. Spectrom*., **2019**, *34*, 1184-1190.

16. Fujiwara, T., Kobayashi, T. & Midorikawa, K. Selective Resonance Photoionization of Odd Mass Zirconium Isotopes Towards Efficient Separation of Radioactive Waste *Sci Rep* **2019**, *9,* 1754.

17. Kowalczyk, P., Gauden P.A., Terzyk, A.P. Cryogenic Separation of Hydrogen Isotopes in Single-Walled Carbon and Boron-Nitride Nanotubes: Insight into the Mechanism of Equilibrium Quantum Sieving in Quasi-One-Dimensional Pores *J. Phys. Chem. B,* **2008**, *112*, 8275 – 8284.

18. Heung, L.K., Sessions, H.T., Xiao, X. TCAP Hydrogen Isotope Separation Using Palladium and Inverse Columns *Fusion Science and Technology*, **2011**, *60,* 1331-1334.

19. Lin, X., Zhu, Q., Leng, H., Yang, H., Luy, T., Li, Q. Numerical Analysis of the Effects of Particle Radius and Porosity on Hydrogen Absorption Performances in Metal Hydride Tank *Appl. Energy*, **2019**, *250*, 1065-1072.

20. Bérubé, V., Radtke, G., Dresselhaus, M., Chen, G. Size Effects on the Hydrogen Storage Properties of Nanostructured Metal Hydrides: A review *Int. J. Energy Res.,* **2007**, *31*, 637-663.

21. Sunandana, C.S. Nanomaterials for Hydrogen Storage, *Resonance*, **2007**, *12*, 31-36.

22. Yen, T.H., Chen, B.H., Chen, B.D. Numerical Simulation and Performance Test of Metal Hydride Hydrogen Storage System *Int. J. of Energy and Environment*, **2011**, *2*, 401-414.

23. Oh, H., Hirscher, M. Quantum Sieving for Separation of Hydrogen Isotopes Using MOFs *Eur. J. Inorg. Chem.* **2016**, 4278–4289.

24. Chen, B., Xiang, S., Qian, G. Metal−Organic Frameworks with Functional Pores for Recognition of Small Molecules *Acc. Chem. Res.* **2010**, *43*, 1115-1124.

25. Kowalczyk, P., MacElroy, J.M.D. Equilibrium Properties of Dense Hydrogen Isotope Gases Based on the Theory of Simple Fluids *J. Phys. Chem. B* **2006,** *110*, 14971-14975.

26. Jin, Y., Wang, L., Hara, M., Watanabe, K. Kinetics of Hydrogen Isotope Absorption for Well-Annealed Palladium-Platinum Alloys *Mater. Trans.* **2007**, *48*, 560-565.

27. Hunyadi Murph, S.E., Larsen, G.; Coopersmith, K. Anisotropic and Shape-Selective Nanomaterials: Structure-Property Relationships *Nanostructure Science and Technology series*, Springer Publisher, **2017**, 1-470.

28. Hunyadi Murph, S.E., Larsen, G.; Lascola, R. Multifunctional hybrid Fe2O3-Au nanoparticles for efficient plasmonic heating *J. Visual Experiments*, **2016**, *108*, 53598.

29. Larsen, G.; Farr, W.; Hunyadi Murph, S.E. Multifunctional Fe2O3-Au Nanoparticles with Different Shapes: Enhanced Catalysis, Photothermal Effects, and Magnetic Recyclability *J. Phys. Chem*. C, **2016**, *120*, 15162-15172.

30. Murphy, C.J.; Sau, T.K.; Gole, A.M.; Orendorff, C.J.; Gao, J.; Gou, L.; Hunyadi, S.E., Li, T. Anisotropic Metal Nanoparticles: Synthesis, Assembly, and Optical Applications *J. Phys. Chem. B* (Feature Article; a Top Five ACS article by citations, National Chemistry Week, 2007), **2005**, *109,* 13857-13870.

31. Hunyadi Murph, S.E., Murphy, C.; Colon-Mercado, H.; Torres, R.; Heroux, K.; Fox, E.; Thompson, L.; Haasch, R. Tuning of Size and Shape of Au-Pt Nanocatalyst for Direct Methanol Fuel Cells *J. Nanoparticle Research*, **2011**, *13*, 6347-6364.

32. Brown, T. L.; LeMay, H. E.; Bursten, B. E.; Murphy, C. J.; Woodward, P. M.; Stoltzfus, M. W., Chemistry: The Central Science. 13th Ed.; *Pearson: Upper Saddle River*, NJ, **2015**.

33. Brown, M., Coopersmith, K., Sessions, H., Ali, M., Murph, S.E. Magnetic Induced Heating of Gold-Iron Oxide Nanoparticles *IEEE Antennas and Propagation Society International Symposium, Proceedings,* **2017,** 903-904.

34. Liao, S., Dourmashkin, P., Belcher, J. W, MIT. Sources of Magnetic Fields, **2004**, http://web.mit.edu/viz/EM/visualizations/coursenotes/modules/guide09.pdf.

35. Jiang, K., Smith, D. A., Pinchuk, A., Size-Dependent Photothermal Conversion Efficiencies of Plasmonically Heated Gold Nanoparticles *J. Phys. Chem. C,* **2013**, *117*, 27073-27080.

36. Fortin, J.P., Wilhelm, C., Servais, J., Menager, C., Bacri, J.C., and Gazeau, F., Size-Sorted Anionic Iron Oxide Nanomagnets as Colloidal Mediators for Magnetic Hyperthermia *J. Am. Chem. Soc.* **2007,** *129* (2628-2635), 2628

37. Lee, J.; Jang, J.; Choi, J.; Moon, S.H.; Noh, S.; Kim, J.; Kim, J.; Kim, I.; Park, K. I.; Cheon, J., Exchange-Coupled Magnetic Nanoparticles for Efficient Heat Induction *Nature Nanotech.* **2011,** *6*, 418-422.

38. Keblinski, P., Cahill, D.G., Bodapati, A., Sulivan, C.R., Taton, T.A. Limits of Localized Heating by Electromagnetically Excited Nanoparticles *Journal of Applied Physics* **2006,** *100*, 054305.

39. Adams, B.D., Chen, A. The Role of Palladium in a Hydrogen Economy *Materials Today* **2011**, *14*, 282-289.

40. Jin, Y., Wang, L., Hara, M., Watanabe K. Kinetics of Hydrogen Isotope Absorption for Well-Annealed Palladium-Platinum Alloys *Materials Transactions* **2007**, *48*, 560-565.

41. Anand, N.S., Pati, S., Jat, R.A., Parida, S.C., Mukerjee S.K. Hydrogen Isotope Effect on Thermodynamic Properties of Pd0.9X0.1 (X = Cu, Ag and Au) Alloys *International Journal of Hydrogen Energy* **2017**, *42*, 3136-3141.

42. Luo, W., Cowgill, D.F., Flanagan, T.B. Separation Factors for Hydrogen Isotopes in Palladium Hydride J. *Phys. Chem. C* **2013**, *117*, 13861−13871.

43. Narayan, T.C, Hayee, F., Baldi, A., Koh, AL, Sinclair, R., Dionne, J.A. Direct Visualization of Hydrogen Absorption Dynamics in Individual Palladium Nanoparticles *Nature Comm.* **2017,** *8*, 14020, 1-8.

44. Li, G.; Kobayashi, H.; Dekura, S.; Ikeda, R.; Kubota, Y.; Kato, K.; Takata, M.; Yamamoto, T.; Matsumura, S.; Kitagawa, H., Shape-Dependent Hydrogen-Storage Properties in Pd

Nanocrystals: Which does Hydrogen Prefer, Octahedron (111) or Cube (100)? *J. Am. Chem. Soc.* **2014**, *136*, 10222-10225.

45. Langhammer, C., Zorić, I., Kasemo, B., and Clemens, B. M., Hydrogen Storage in Pd Nanodisks Characterized with a Novel Nanoplasmonic Sensing Scheme *Nano Lett.* **2007**, *7*, 3122-3127.

46. Baldi, A., Narayan, T.C., Koh, A.L, Dionne, J.D. In Situ Detection of Hydrogen-Induced Phase Transitions in Individual Palladium Nanocrystals *Nature Materials* **2014**, *13*, 1143-1148.

47. Belkhiria, S., Briki, C., Dhaou, M.H., Sdiri, N., Jemni, A., Askri, F., Nasrallah S.B. Experimental Study of Metal-Hydrogen Reactor Behavior During Desorption under Heating by Electromagnetic Induction *International Journal of Hydrogen Energy* **2017**, *42*, 16645-16656.

48. Sandeep, K.C., Shinde, S.S., Mistry, K., Bhanja, K., Mohan, S., Mandal, D., Mahajani, S. Adsorption Kinetics on the Recovery of Hydrogen Isotopes from Helium using Palladium Particle Bed *International Journal of Hydrogen Energy* **2017**, *42*, 29300-29309.

Table Of Contents (TOC) graphic

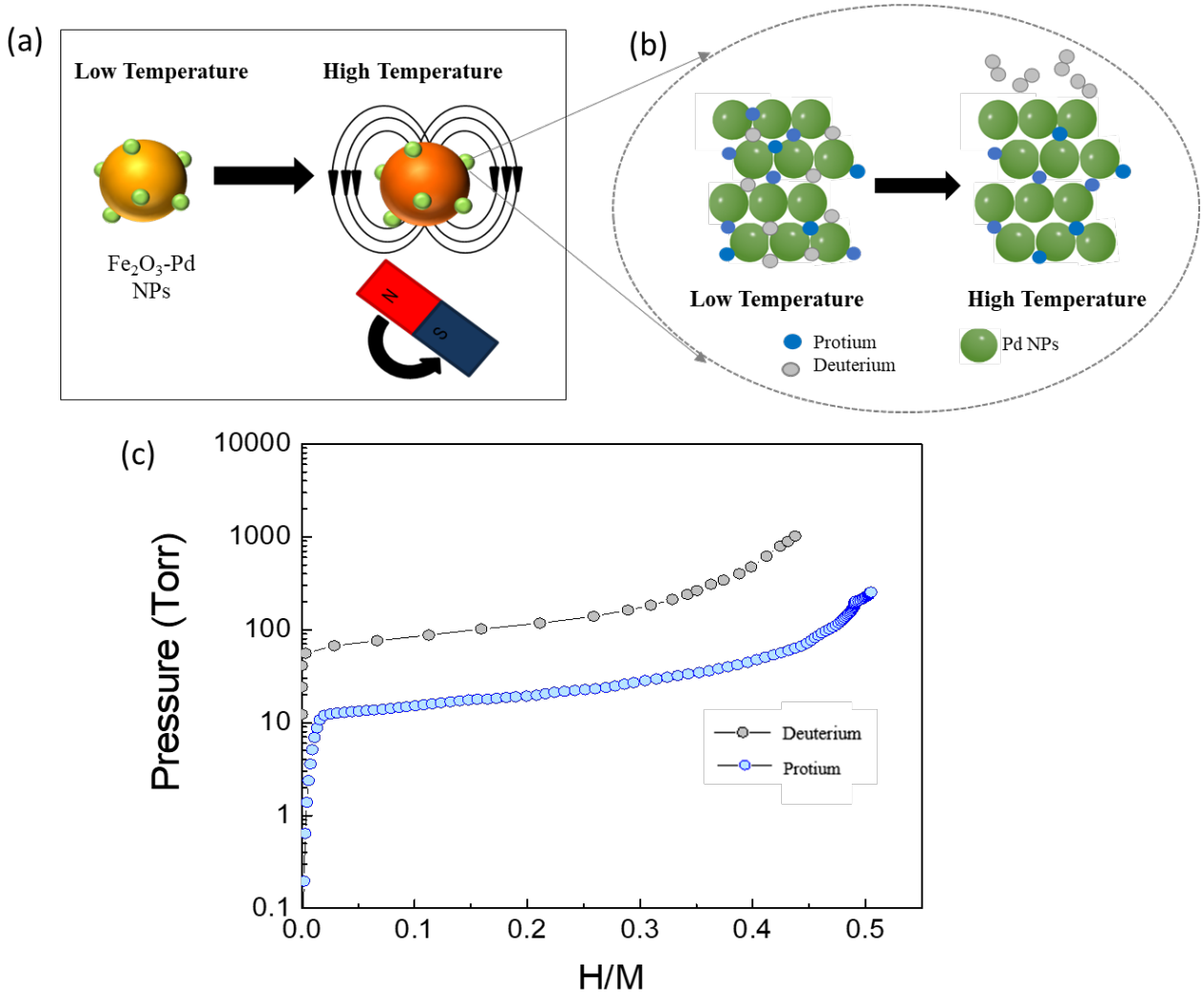

(a) *Energy, in the form of an alternating magnetic field, is selectively coupled to Fe_2O_3-Pd NPs. The Fe_2O_3 component of the Fe_2O_3-Pd NPs act as a local "hot-spot" and heat up the surrounding media;*

(b) *Illustration showing hydrogen (protium and deuterium) absorption/desorption process by palladium at different temperatures;* ***(c)*** *Protium (blue) and deuterium (gray) pressure-composition absorption isotherms for Fe_2O_3-Pd NPs at room temperature.*